Insights into molecular imprinting polydopamine *in-situ* activating peroxydisulfate for targeted removal of refractory organic pollutants: Overlooked N site

Min Tang [a], Jinquan Wan [a,b,*], Yan Wang [a], Gang Ye [a], Zhicheng Yan [a], Yongwen Ma [a], Jian Sun [a]

[a] *School of Environment and Energy, South China University of Technology, Guangzhou 510006, China*
[b] *State Key Laboratory of Pulp and Paper Engineering, South China University of Technology, Guangzhou 510640, China*

A B S T R A C T

This study proposed a simple and green method to develop a molecular imprinting polymer for *in-situ* activating peroxydisulfate (PDS) without metal active sites and then targeted degrading pollutants. The molecularly imprinted polydopamine (MI-PDA) can selectively re-bonded target pollutant (sulfamethoxazole, SMX) by nitrogenous and oxygenated functional groups. On this basis, the N site of nitrogenous groups can efficiently *in-situ* activate PDS to generate singlet oxygen ($^1O_2$). The detailed mechanism is that PDS adsorbed on the electron-deficient N site of MI-PDA would transfer the electron to the N atom in MI-PDA, shorting the O-O bond length and resulting in the cleavage of S-O bond of PDS, which induced more $^1O_2$ generation. Tow functions, selective enrichment and *in-situ* activation, endowed MI-PDA/PDS system with over 95% removal efficiency of SMX and 9.23-fold enhancement of degradation rate constants. This work provided novel insights into the selective removal of target pollutants in complicated water matrix.

1. Introduction

Trace refractory organic pollutants in water have aroused wide public concern due to the removal resistance of conventional methods [1–4]. Persulfate-based advanced oxidation processes (AOPs) are defined as an effective way to eliminate refractory organic pollutants owing to the high redox potential of the generated radicals [5–7]. Currently, one of the most adopted activation approaches for peroxydisulfate (PDS) is the use of heterogeneous catalysts, including transition metals, metal oxides, and metal-free materials [8]. Metal-free catalyst has been intensively exploited in activating PDS due to the effective activation and environmental friendliness [9]. However, the poor selectivity for trace refractory organic pollutants often leads to a sharp drop in the removal efficiency under interference from competitive pollutants [10]. Even the surfeit free radical cannot assure the high removal rate of refractory organic pollutants, as the short half-life of free radical ($SO_4^{\bullet-}$ < 40 µs, •OH < 20 ns) and the low concentration of refractory organic pollutants in water [11,12]. Recently, several studies found that conjugating molecularly-imprinted polymer with AOPs can improve the removal efficiency of trace refractory organic pollutants by enhancing the selectivity of the catalysts toward target contaminants

[13–15]. With respect to the polymer materials, there remains a great space for the exploration of more environmental and efficient polymer materials as potential metal-free catalyst for PDS activation.

While nearly all reported molecularly imprinted catalysts were engineered by constructing a molecularly imprinted layer on the surface of an intrinsic catalyst [16–19]. Li et al. synthesized a molecularly imprinted layer on the surface of the Fe-metal-organic framework (MIL100) using the surface imprinting method, resulting in the diethyl phthalate (DEP) removal of 105.2 mg/g [20]. Yuan et al. designed a molecularly imprinted layer on graphite carbon nitride nanosheets for selective photocatalytic degradation of extracellular antibiotic resistance genes (bla_{NDM-1}) in secondary effluent. The introduction of molecularly imprinted layer enhanced the degradation of bla_{NDM-1} by improving the utilization of photogenerated oxidizing species [21]. Importantly, the preparation process of traditional molecular imprinting catalysts is complicated due to the addition of crosslinking agent, functional monomer, initiator and catalytic material [22–24]. This challenge underscores the need to develop a simple method used to prepare molecular imprinting. Intrinsically, the introduction of molecularly imprinted layers would hamper the mass transfer of oxidants and reactive oxygen species (ROS), thus the role of molecular imprinting has

not been fully utilized [15,25]. Moreover, the binding between the catalytic materials and the imprinting layer needs to be considered because the physical encapsulation is not conducive to the synergy of the adsorption in imprinting layer and the catalysis in catalytic materials. Therefore, the *in-situ* activation of PDS by molecularly imprinted polymers is worth further discussion. At present, there is no report on the study of one-step construction of molecularly imprinted polymers for *in-situ* activating PDS. This molecular imprinting polymer with *in-situ* activating PDS is less susceptible to the interference of the synergistic effect between the catalytic materials and the imprinting layer, the inhibition of PDS mass transfer, and the release of toxic metals.

Inspired by the adhesive properties of mussel foot proteins, polydopamine (PDA) has been attracting huge interest in fields like energy storage, catalysis, biosensors, drug delivery, and environmental remediation [26–30]. Due to the mild and environmentally benign synthesis and self-polymerization property [31], PDA may be a candidate for the synthesis of molecularly imprinted materials without the addition of crosslinking agent and initiator. Meanwhile, the functional groups such as -NH$_2$ and -OH in dopamine (DA) are easy to combine with various groups [32], thus all kinds of target pollutants can interact with DA to form the recognition sites. Moreover, it was reported that the addition of PDA can promote the activation efficiency of catalyst toward oxidants, which is inseparable from the formed quinones in PDA [33]. Therefore, it is feasible that molecularly imprinted PDA *in-situ* activate PDS. The underlying mechanisms of pure PDA activating PDS need to explored either.

In this study, it was for the first time to systematically explore the mechanism and effect of activation PDS degradation by PDA as molecularly imprinted material. The primary concerns of this study were to verify the following questions: (1) can PDA suit for constructing the imprinted recognition sites; (2) can PDS be activated by imprinting modified PDA to generate ROS; (3) what is the underlying mechanism of the PDA as the molecular imprinting polymer activating PDS. Firstly, the molecular dynamics simulation was applied to testify the theoretical feasibility of PDA forming molecular imprinting materials, and then prepared the green molecular imprinting catalyst (MI-PDA). The selective adsorption performance of MI-PDA was compared with non-imprinting PDA (NI-PDA) to reveal the actual feasibility of specific recognition. Degradation experiments were conducted to prove the *in-situ* catalytic performance of MI-PDA toward PDS. Electron paramagnetic resonance (EPR), quenching experiment and molecular probe experiment were used to confirm the key role of $^1O_2$. The mechanism of MI-PDA activating PDS to produce $^1O_2$ was investigated from the perspectives of density functional theory (DFT) calculation and *in-situ* ATR-FTIR. This study not only provides a green and simple synthesis method for molecular imprinting formation but also put forward new insights into the generation of $^1O_2$ by PDA activating PDS.

2. Materials and methods

2.1. Chemical reagents

Dopamine (DA), sulfamethoxazole (SMX), ciprofloxacin (CPI), tetracycline (TET), enrofloxacin (ENF), tert butyl alcohol (TBA), furfuryl alcohol (FFA), benzoquinone (BQ), benzoic acid (BA), phenol, *L*-histidine, K$_2$Cr$_2$O$_7$, ammonia aqueous solution (NH$_4$OH, 28–30%), benzoic anhydride (BAD), 2-bromo-1-phenylethanone (BrPE), 1,3-diphenylisobenzofuran (DPBF), KI, NaHCO$_3$, Na$_2$SO$_4$, NaCl, NaNO$_3$, Na$_2$CO$_3$, sulfadiazine (SDZ), sulfapyridine (SPD), atrazine (ATZ), primidone (PMD), metronidazole (MDE) and deuterium oxide (D$_2$O) were purchased from Sigma-Aldrich. Methyl alcohol (MeOH), ethyl alcohol (EtOH), acetic acid, CHCl$_3$, and ammonium hydroxide were supplied by Kemiou Chemical Reagent (Tianjin, AR). All the above reagents were analytic reagents. Deionized (DI) water used throughout the experiments was obtained from the laboratory purification system.

2.2. Preparation of MI-PDA

Ammonia aqueous solution (0.75 mL) was mixed with ethanol (40 mL) and deionized water (90 mL) under mild stirring (400 rpm) at 25 °C for 30 min. SMX (0.05 g) as the template molecular was added into the above solution with stirring at room temperature for 10 min. DA (0.50 g) was dissolved in DI water (10 mL) and then injected into the above mixture solution. The color of this solution immediately turned pale brown and gradually changed to dark brown. The reaction was allowed to proceed for 30 h.

The products were collected by centrifugation and eluted the template of SMX was with methanol/acetic acid (9:1, v/v) mixed solvent for 12 h, and then washed with methanol and DI water until no SMX was detected in the supernatant. Finally, these products were vacuum dried under 60 °C for 12 h. The prepared materials were referred to as MI-PDA. For comparison, the non-imprinted catalyst (NI-PDA) was prepared with the same method as described above, except that SMX was omitted. The prepared process of MI-PDA can be seen in Scheme S1.

The masking of oxygen-containing functional groups in MI-PDA catalyst was shown in *Text S1*.

2.3. Characterization

The morphology and structure of prepared materials were observed by high-resolution field emission scanning electron microscope (FESEM, NOVA NANOSEM 430) and transmission electron microscopy (TEM, Talos F200X). The surface area and pore distribution of prepared materials were measured by N$_2$ adsorption using a Micromeritics ASAP 2460 surface area analyzer. The chemical structure of the material surface was characterized by attenuated total reflection Fourier transform infrared (ATR-FTIR, Thermo iS50) and X-ray photoelectron spectroscopy (XPS, Kratos Axis Ultra DLD). High-Performance Liquid Chromatography (HPLC, Shimadzu LC-20A) was used to test the pollutant concentration. The intermediate products in the SMX degradation process were detected *via* liquid chromatography-mass spectrometry (LC-MS, Agilent 1290UPLC-QTOF6550). The electrochemical performance was measured *via* electrolyte for cyclic voltammetry (CV) using an electrochemical analyzer in a standard three-electrode system with the prepared materials as the working electrode. In the measuring process, 0.1 M NaSO$_4$ was used as an electrolyte. Electron paramagnetic resonance (EPR) spectra were obtained using a Bruker EPR A200 spectrometer at room temperature for analyzing the species of ROS.

In-situ ATR-FTIR measurements were performed using a Thermo Scientific Nicolet iS10 FTIR spectrophotometer equipped with a multi-bounce horizontal ATR accessory and flow cell (Pike Technologies). All the spectra were recorded in a range of 4000–600 cm^{-1} with 128 scans. A horizontal Ge ATR crystal was coated with a film by drying the MI-PDA suspension (2.0 g/L). The adsorbed solution was pumped using a peristaltic pump at a rate of 0.5 mL•min^{-1}. Before the adsorption experiments, a background spectrum was firstly collected as the MI-PDA catalyst deposit was equilibrated with ultrapure water. All spectra were recorded at the pre-determined time and the total acquisition time was 60 min. Then 0.05 g PDS was added to the adsorbed solution. Spectra were collected immediately after the solution passed through the MI-PDA catalyst deposit and then all spectra were recorded at the pre-determined time and the total acquisition time was 60 min. After the catalyst experiments, the MI-PDA film was checked to ensure no erosion. All the fitted IR spectra were compared on the same scale.

2.4. Selective adsorption and catalytic experiment

Static adsorption and catalysis experiments were carried out with single pollutant simulating wastewater of SMX. 0.05 g of as-prepared material and 100 mL wastewater containing different concentrations of SMX were added into a conical flask. After adsorption equilibrium, 2.0 mM PDS was put into wastewater to trigger advanced oxidation

process. As the reaction proceeded, 1.0 mL aliquots of reaction solution were withdrawn by syringe at designated time intervals, and immediately filtered through a Millipore filter (0.22 μm), followed by High Performance Liquid Chromatography (HPLC) analysis of the residual SMX concentration.

Selective adsorption experiments were conducted in mixed solution containing the different concentration of CPI, TET, ENF, and SMX. The specific method was the same as the above adsorption process. Finally, the residual concentrations of different pollutants (CPI, TET, ENF, SMX) were detected respectively by HPLC. The HPLC analysis of CPI, TET, ENF, and SMX was showed in *Text S2*.

Imprinting factor (IF) and selectivity coefficient (SC) were used to evaluate the selective recognition ability. IF and SC can be calculated by the following equations:

$$IF = \frac{Q_{MIC}}{Q_{NIC}}$$

$$SC = \frac{IF_T}{IF_C}$$

Here, Q_{MIC} and Q_{NIC} (mg/g) are the adsorption capacities of MI-PDA and NI-PDA for SMX, respectively. IF_T and IF_C are the imprinting factor of MI-PDA for the template (SMX) and competitions (TET, CPI, ENF), respectively.

Details of water samples (tap water, river water, pharmaceutical wastewater) used in actual water systems are presented in the *Text S3* and Table S2.

Quenching experiments are showed in *Text S4*. PDS concentration measurement is displayed in *Text S5*. $^1O_2$ concentration was measured as shown in *Text S6*.

2.5. Theoretical calculations

Molecular dynamics simulations of all atoms were performed under Windows system using the Material Studio software package (Accelrys). COMPASS force field was used to construct and simulate the molecular imprinted preassembly system[34]. The main modules were set as follows: On the Amorphous Cell module, the calculation accuracy was set to fine and the frame was set to 1. Forcefield was compass and the charge was set to Forcefield assigned, and the summation methods were Group based and Edward. The Dmol3 module was set with GGA-PerdeW-Burke-Ernzerhof correlation, and the TS method was used for DFT-D correction.

The Forcite module is used for annealing to explore the conformational space of the global low-energy structure by periodically increasing and decreasing the temperature of the classical kinetic trajectory. The monomer-template ratio was 40:10 (n/n). In the Forcite module setting, the annealing process adopts 100 annealing cycles, the time step is 1fs, and the temperature is set at 300–600 K. There are 10 heating and cooling cycles per cycle to make the temperature change in a uniform manner. The NVT ensemble is used for quenching and annealing to simulate water bath conditions.

After annealing, the three configurations with the lowest energy of the system were selected for quenching treatment. Based on the annealing optimization, the local potential energy changes were combined with the template in different directions and positions to obtain a more stable low-energy conformation. The average value of binding energy was calculated by selecting the energy structure of three pollutant-monomers with the lowest energy. The calculation formula is:

$$E_{binding} = E_{total} - E_{template} - E_{monomer}$$

Where, $E_{binding}$ is the binding energy between template molecules and monomer, E_{total} is the total energy of the system, $E_{template}$ is the molecular energy of template, and $E_{monomer}$ is the total energy of monomer.

The electronic density difference (EDD) analysis and transition state (TS) search were calculated using CASTEP and DMol3 modules of Material Studio software package (Accelrys), respectively. The configuration is firstly optimized with the corresponding module.

3. Results and discussion

3.1. Characterization

As shown in Fig. 1, the MI-PDA exhibited a nanosphere structure with the size of 610 ± 6 nm. The surface of MI-PDA was rougher than that of NI-PDA, which was ascribed to the formation of imprinted cavities (Fig. S1). The HRTEM images displayed the solid nanospheres of MI-PDA, and the uniform distribution of C, O, and N elements indicated the complete elution of templates (SMX) with S as the characteristic element (Figs. 1b-1c). Two new types of pores appeared at 2.5 nm and 3.5 nm in the MI-PDA pore distribution (Fig. 1d) compared with NI-PDA, indicating the formation of imprinted cavities. This result also can be testified by the surface area and pore volume (Fig. S2), detailly, the BET surface area (10.07 m²/g) and BJH pore volume (0.03 cm³/g) of MI-PDA were lager than that of NI-PDA with 8.40 m²/g and 0.02 cm³/g, respectively.

The chemical structure of the catalyst materials has a great influence on adsorption and degradation performance. The typical N 1 s signal is corresponds to nitrogen species in the MI-PDA. In the N 1 s spectrum of MI-PDA (Fig. 1e), the peaks of −N = (399.1 eV) and -NH- (400.0 eV) are correspond to the cyclized nitrogen in the indole units [27]. Meanwhile, the signal peak of-NH₂ located at 400.7 eV confirms the existence of open-chain oligomers in MI-PDA aggregates. The O 1 s (Fig. 1f) and C1s (Fig. S3) signals of MI-PDA can prove the C–O, C-O-C, and C=O species. ATR-FTIR spectrum further characterized the groups in the MI-PDA. The peaks of 1250, 1480, 1500, 1610, and 3200–3500 cm⁻¹ are assigned to C-N, amide, amide II, aromatic rings, and -NH-/-OH groups, respectively (Fig. S4). XRD spectrum showed broad diffraction peak at 22.3°, which is correspond to the graphite carbon (002) crystal plane (Fig. S5). The structure of MI-PDA is similar to the carbon frameworks with sp² hybridization [35]. All results confirmed that the molecular imprinted cavities were successfully constructed in the polydopamine.

3.2. Feasibility analysis of MI-PDA formation recognition site

Molecular dynamics was used to infer the pre-polymerization feasibility between dopamine monomers and template molecules (SMX). After 50 times cycles, a stable configuration on the 35th cycle with lowest energy can be obtained (Fig. S6), which was chosen as the model for further investigation. As shown in Fig. 2a, DA can bond with SMX through hydrogen bonds rather than chemical bonds. The appearance of red shifts in UV–vis spectrophotometer resulted in the decrease of the electronic transition energy of imprinting system [17], which further confirmed the weak interactions between the DA and SMX (Fig. S7), such as hydrogen bond. The formation of weak interactions indicates that SMX can elute after polymerization to leave imprinted cavities. Quantum mechanical analysis was thus performed on the electron cloud density to explore the possible interaction between the benzene rings in SMX and DA [34]. Overlapping electron clouds were observed between the benzene rings of DA and SMX (Fig. 2b), indicating that the π-π conjugation of the benzene rings was the bonding way of DA and SMX. The calculation of the energy within the imprinting system (Table S1) demonstrates that the van der Waals and electrostatic forces were contributed most to the selective adsorption. The van der Waals and electrostatic forces respectively indicated that π-π conjugation and extensive hydrogen bonding were involved in the imprinting system. The results indicated that DA was easy to bind with the SMX to form imprinting recognition sites. Hence, DA was a compatible monomer for the molecular imprinting polymer.

To verify the selectivity of the recognition sites, concentration-dependent selective adsorption experiments in simple system (Fig. 2c)
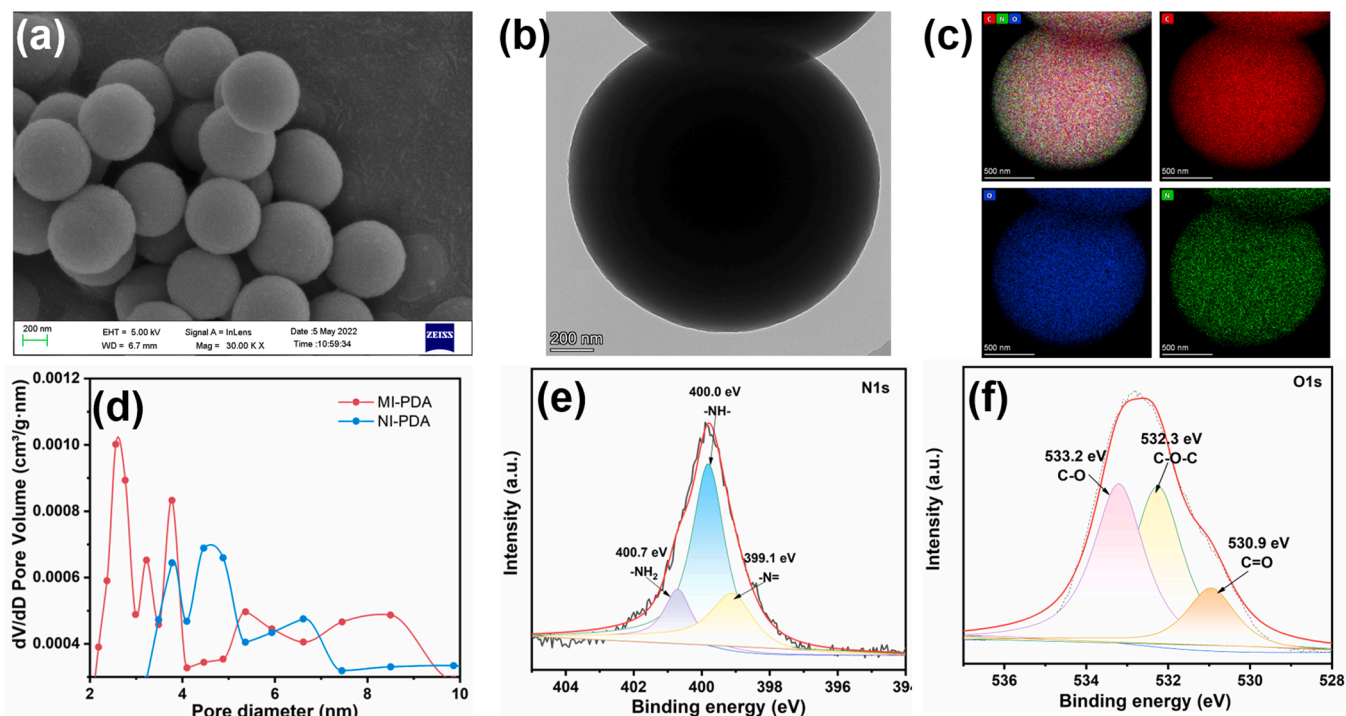
Fig. 1. (a) SEM images, (b) TEM images, and (c) TEM-EDS-mapping of MI-PDA. (d) The pore distribution of NI-PDA and MI-PDA. (e) N 1 s and (f) O 1 s spectrum of MI-PDA.

and coexistent system (Figs. 2d-2e) were performed on MI-PDA and NI-PDA using TET, CIP and ENF as non-targets. In simple system, the increase of template dosage in polymerization process can enhance the adsorption capacity of MI-PDA, which was attributed to the formation of abundance of recognition sites. While too many template molecules would weaken the adsorption capacity because the overlap of the large number of template molecules resulted in the mismatch between template molecules and the shape of imprinted cavity formed after polymerization-elution (Fig. S8). As shown in Fig. 2a, MI-PDA shows higher re-bonding capacity towards the SMX than the NI-PDA, which was ascribed to the prominent role of recognition site in MI-PDA. Interestingly, the IF values decreased with the SMX concentration increased from 0.2 mM to 3.2 mM, indicating the molecular imprinting technology is more suitable for the removal of micropollutants. In the coexistent system, the concentration of non-targets was 1.0 mM, the concentration of SMX increased from 0.2 to 1.0 mM. It can be found that MI-PDA shows the highest adsorption capacity toward target (SMX) than non-targets, exhibiting the selectivity. While the adsorption capacity of NI-PDA toward four pollutants has no obvious priority (Fig. 2d). As seen in Fig. 2e, IF values toward SMX of MI-PDA is higher twice than that toward no-targets. Importantly, the SC values declined with the SMX concentration increasing, which further demonstrates the feasibility of treating micropollutants of MI-PDA. These results confirmed the feasibility of DA as a monomer to form molecularly imprinted polymers for selective re-bonding targets. Table 1.

3.3. In-situ activation of PDS by MI-PDA to selectively degrade SMX

A large number of molecularly imprinted polymers require additional construction of active sites to activate PDS [14,36]. *In-situ* activation of PDS by molecularly imprinted polymers to degrade pollutants has not been reported. The reactivities of MI-PDA were evaluated by activating PDS to degrade SMX. Fig. 3a shows that the removal efficiency of SMX by the only PDS and MI-PDA were 10% and 8%, respectively. Interestingly, SMX degradation was effectively enhanced to 95% by coupling MI-PDA and PDS, suggesting the activation

performance of MI-PDA. With the catalyst dosage increase, the SMX removal was enhanced (Fig. S9), which was because higher catalyst dosages are thought to give more active sites for activating PDS and creating more reactive species. MI-PDA displayed widespread reactivity for activating PMS and H_2O_2 (Fig. S10). As displayed in Fig. 3b, compared with the typical sp2 hybrid carbon materials (CNT-OH), the degradation rate constant (k_{obs}) of MI-PDA enhanced 2.80-fold, suggesting that MI-PDA can be acted as a metal-free catalyst. Importantly, the k_{obs} value of MI-PDA is 9.23 times that of NI-PDA, which was attributed to the enrichment of SMX by the priority re-bonding performance of recognition sites. MI-PDA shows a faster degradation rate than our previous study about molecularly imprinted catalyst with extra metal active center [37], demonstrating that the superiority of *in-situ* activation of the molecularly imprinted polymer catalyst.

Due to the selective re-bonding of recognition site, the MI-PDA/PDS system exhibits oxidation selectivity in coexistent system. As shown in Figs. 3c-3d, NI-PDA exhibits analogical and weak degradation capacity (below 70%) toward the four antibiotics in different concentration, while MI-PDA is prone to degrading SMX and removal capacity toward SMX achieves above 90%, owing to the selective pre-adsorbing. Interestingly, MI-PDA exhibited similar adsorption and degradation efficiency toward the homologue of SMX such as sulfadiazine (SDZ) and sulfapyridine (SPD) (Fig. S11), indicating that MI-PDA catalyst can selectively remove homologous pollutants. MI-PDA displays obvious selectivity in both adsorption and degradation processes. As expected, as the SMX concentration increased, the ability of specific adsorption of recognition site was weakened, resulting in the slight decline of SMX removal. In the actual water environment, the concentration of refractory pollutant was significantly lower than that of the distractors, hence, molecularly imprinted polymer catalysts have the potential to treat trace refractory organic pollutants in water.

3.4. Determination of ROS and the mechanism for activating PDS

To further reveal the mechanism of MI-PDA activating PDS, the EPR test and quenching experiments of active species were conducted. As
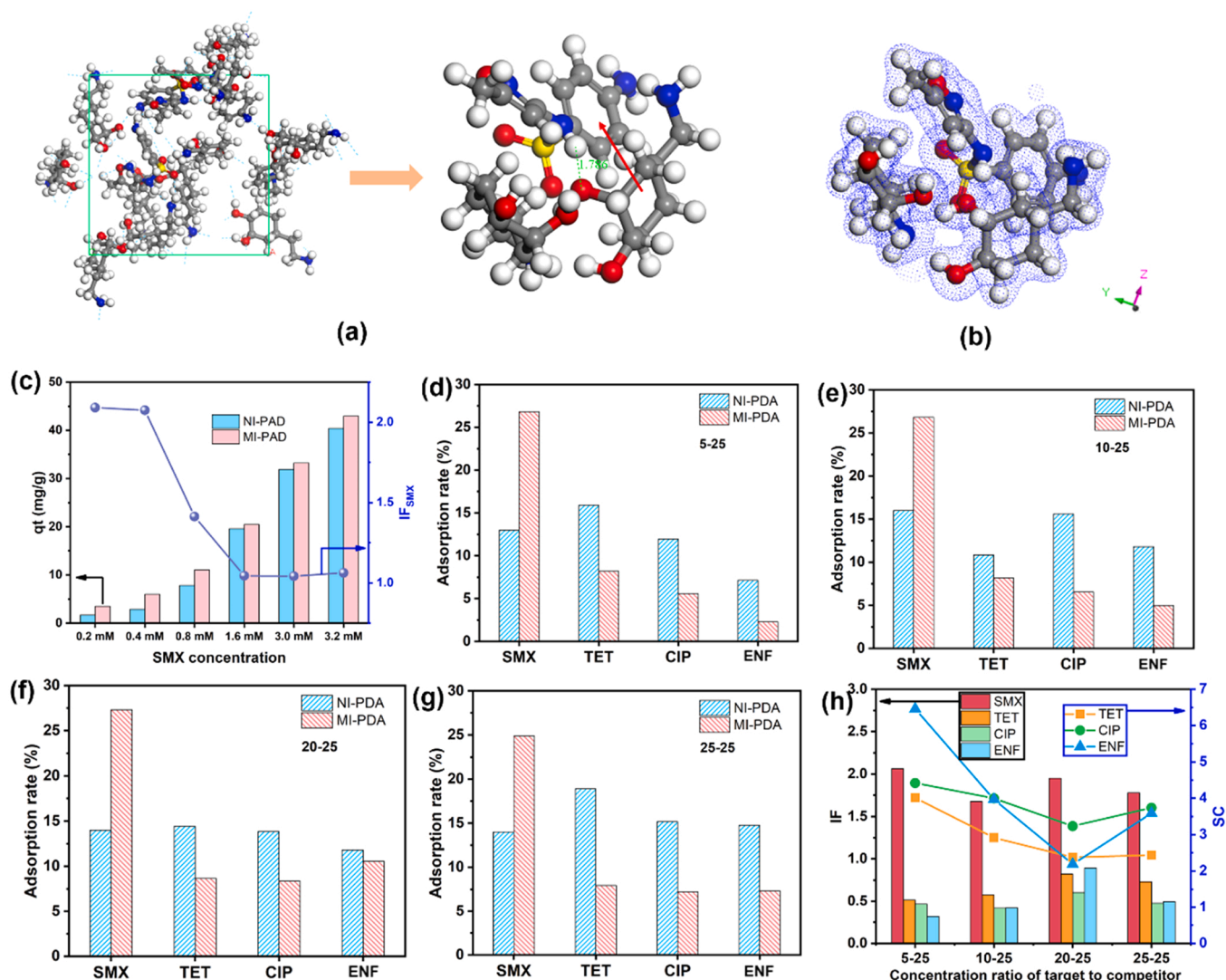
Fig. 2. (a) The hydrogen bond of DA-SMX imprinting system in optimization structure. (b) Electron cloud density analysis of DA-SMX system. Adsorption capacity of MI-PDA and NI-PDA toward SMX in simple system (c) and coexistent system with the different concentration of (d) 5–25, (e) 10–25, (f) 20–25, and (g) 25–25. (h) The IF and SC values of MI-PDA in coexistent system. 5–25, 10–25, 20–25, and 25–25 mean that the concentration of SMX is 0.2, 0.4, 0.8, and 1.0 mM and the concentration of other pollutants is 1.0 mM. Reaction conditions: [Catalyst] = 0.5 g/ L, T = 25 °C, initial pH = 6.8.

Table 1
the selectivity of MI-PDA in adsorption and degradation process.

System	Target		Q_e (mg/g)		IF
			MI-PDA	NI-PDA	
Simple	Adsorption	SMX	11.04	7.81	1.41
		CIP	1.52	3.99	0.38
	Degradation	SMX	36.90	25.50	1.45
		CIP	23.44	27.39	0.86
Coexistence	Adsorption	SMX	10.50	7.15	1.47
		CIP	0.78	8.10	0.10
	Degradation	SMX	34.79	13.40	2.60
		CIP	22.06	22.01	1.00

Note: [SMX] = 0.4 mM, [CIP] = 0.4 mM, [Catalyst] = 0.5 g/L. The simple system has only one pollutant, while coexistence system consists of SMX and CIP.

shown in Fig. 4a, compared with PDS, a remarkable characteristic signal of TEMP-$^1O_2$ were appeared in MI-PDA/PDS system, suggesting that MI-PDA is capable of activating PDS to generate $^1O_2$. The pronounced difference in the peak intensities as the reaction time goes attests that MI-PDA definitely gives rise to the production of $^1O_2$ in the PDS activation process. In addition, the characteristic signals referred to the DMPO-•OH, DMPO- $SO_4^{\bullet-}$ (Fig. 4b), $O_2^{\bullet-}$ (Fig. 4c) can also be observed in MI-PDA/PDS system, while the intensity of the characteristic signals have no obvious enhance as reaction time goes, reflecting a limited formation of •OH, $SO_4^{\bullet-}$, and $O_2^{\bullet-}$ in the MI-PDA/PDS system. EPR result preliminarily confirms that $^1O_2$, •OH, $SO_4^{\bullet-}$, and $O_2^{\bullet-}$ may generate from the MI-PDA/PDA system.

To further identify the ROS involved in the MI-PDA/PDS system, quenching tests were performed by utilizing ethyl alcohol (EtOH), tert-butyl alcohol (TBA), benzoquinone (BQ), and L-histidine to scavenge $SO_4^{\bullet-}$, •OH, $O_2^{\bullet-}$, and $^1O_2$ respectively. As shown in Fig. 4d, k_{obs} drops dramatically from 0.044 min^{-1} to 0.005, 0.004, and 0.011 min^{-1} in the absence of •OH, $SO_4^{\bullet-}$, and $O_2^{\bullet-}$, respectively. The removal efficiencies of SMX were decreased to 35%, 34%, and 58% when EtOH, TBA, and BQ respectively injected in the MI-PDA/PDS system (Fig. S12). Considering that L-histidine would consume PDS [38,39], $^1O_2$ quenching experiment was performed after supplementing the PDS consumed by L-histidine. Significantly, the k_{obs} was significant decreased to 0.0012 when L-histidine is added with a high dose (Fig. 4d and Fig. S13). As a result, the SMX oxidation was rely on radicals while the contribution of $^1O_2$ was non-negligible. FFA was recently selected as scavenger of $^1O_2$ due to its
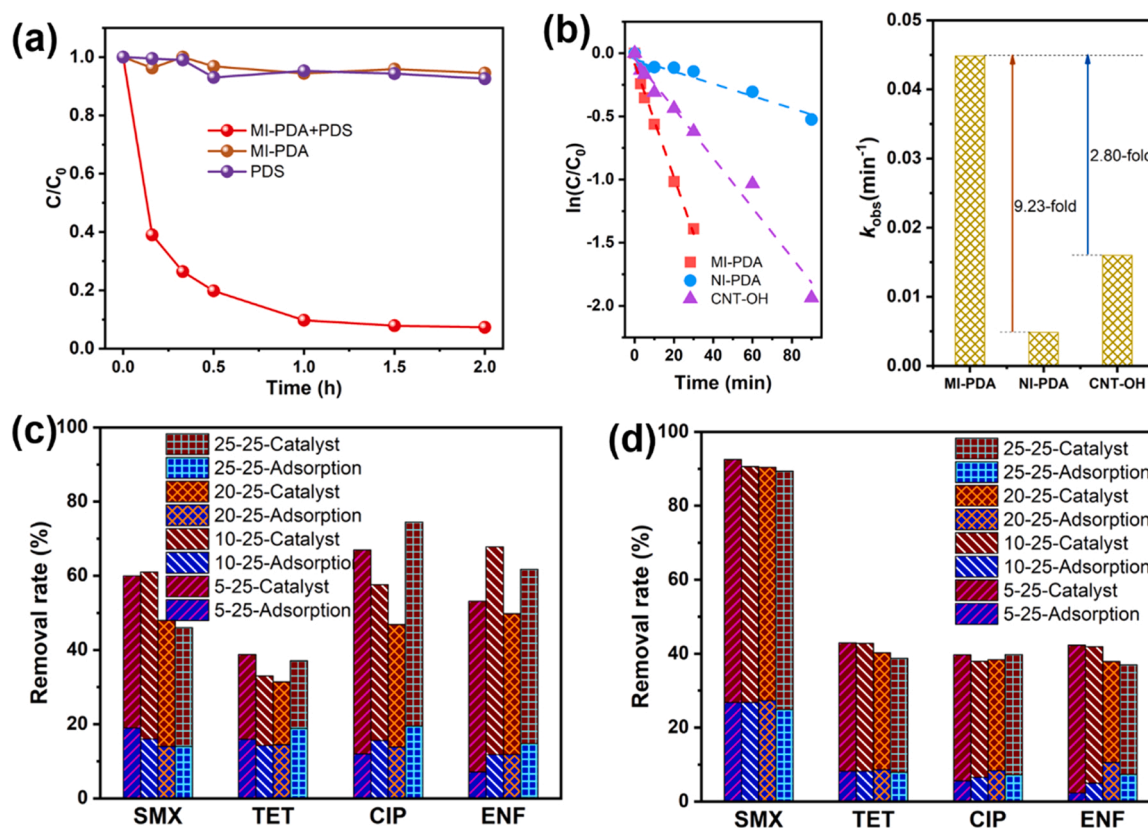
Fig. 3. (a) Removal of SMX in MI-PDA, PDS, and MI-PDA coupling with PDS systems. (b) Kinetic studies of various samples in PDS activation for degradation of SMX in the simple system, [SMX] = 0.4 mM. (c) Removal rate of SMX by NI-PDA/PDS and (d) MI-PDA/PDS in the coexistence system. 5–25, 10–25, 20–25, and 25–25 mean that the concentration of SMX is 0.2, 0.4, 0.8, and 1.0 mM and the concentration of other pollutants is 1.0 mM. Reaction conditions: [Catalyst] = 0.5 g/ L, [PDS] = 2 mM, T = 25 °C, initial pH = 6.8.

high reactivity with $^1O_2$ ($k_{FFA} = 1.2 \times 10^8\ M^{-1}s^{-1}$) [40]. When different concentrations of FFA were injected, the SMX degradation was significantly inhibited (Fig. S14) and the inhibitory effect enhanced with increased FFA concentration. It was reported that FFA not only could react with $^1O_2$ but •OH ($k_{•OH, FFA} = 1.5 \times 10^{10}\ M^{-1}\ S^{-1}$) [15]. When the FFA was injected after the •OH quenching, the SMX degradation was further inhibited (Fig. S15), indicative of the key role of $^1O_2$ in MI-PDA/PDS system. This result is consistent with the EPR result. It was reported that electron transfer as a feasible pathway can oxidate organic pollutants without involvement of ROS. It was reported that premixing can verify electron transfer [41,42]. The premixture experiments of MI-PDA and PDS were conducted to exclude the influence of electron transfer on the oxidation of SMX. If the electron transfer involved in the degradation process, premixture of MI-PDA and PDS have no impact on the SMX degradation. However, as shown in Fig. 4e, the removal of SMX is weakened to 80% with the premixing 10 min, and the decline of SMX removal is more significant as a longer premixing time (Fig. S16). In addition, the one-electron reduction of PDS inherently initiates the generation of reactive oxygen species (SO$_4^{•-}$, •OH, $^1O_2$ and O$_2^{•-}$), therefore K$_2$Cr$_2$O$_7$ was used to quench the solution-phase electron to inhibit the possible ROS generation [42]. K$_2$Cr$_2$O$_7$ addition sharply restrains the SMX degradation in MI-PDA /PDS system (Fig. 4f), suggesting the key contribution of ROS. With the PDS dosage increasing, the SMX degradation efficiency enhanced (Fig. S17), and the PDS can be decomposed with or without SMX in the reaction solution (Fig. S18), which further negates electron transfer form pollutant to PDS. Furthermore, the new anodic peak and the obviously enhanced current of the MI-PDA electrode as the addition of PDS in the cyclic voltammetry (CV) plots and the chronoamperometry (CP) curve (Fig. S19 and Fig. S20) provide additional evidence for the electron transport from PDS to the MI-PDA,

meaning PDS oxidation as the dominant reaction in the course of MI-PDA activating PDS.

Previous study reported that the degradation capacity of a $^1O_2$-dominnated system would be enhanced in the presence of D$_2$O because of the distinct extension of the lifetime of $^1O_2$ (k = $1.6 \times 10^4\ s^{-1}$) [43]. As depicted in Fig. 4g, the SMX removal by the MI-PDA/PDS system is evidently enhanced in D$_2$O than that in H$_2$O. Moreover, the effect of oxygen in air on the determination of ROS is investigated by continuously pumping N$_2$ into the reaction system. An improvement of SMX degradation can be observed (Fig. 4g) with N$_2$ introduction, while no distinguishable varication of SMX degradation occurred in the MI-PDA/PDS system when aerate O$_2$, implying the negligible contribution of oxygen for $^1O_2$ generation. The enhancement of SMX degradation as the N$_2$ pumping is attributed to the acceleration of oxidant dissolution and mass transfer by microbubbles. While too much O$_2$ injection can loot hydrogen bond receptor at the recognition site in the molecular imprinting layer because the O in the O$_2$ can interact with H in sp^2 C−H to form the hydrogen bond to a certain extent [44]. Although the pumping of O$_2$ also accelerated the mass transfer of oxidants, the obstruction of the targeted adsorption process made the addition of O$_2$ have no obviously positive effect on the degradation of SMX. ROS molecular probe experiments were used to further identify the decisive role of $^1O_2$ in SMX degradation. Phenol is prone to degrading by radicals and non-radicals such as $^1O_2$ due to the electrophilicity, while BA can only be degraded by radicals [45]. As shown in Fig. 4h, the phenol removal is higher than BA. Moreover, DPBF as a molecular probe reacts with $^1O_2$ to form an irreversible Diels-Alder 1,4-cycloaddition reaction to quantify the yield efficiency of $^1O_2$ [46]. The concentration of $^1O_2$ is more over 65%. Furthermore, the probe-based kinetic modelling approach studied by Gao [15] was used to evaluate the role of $^1O_2$ in SMX abatement
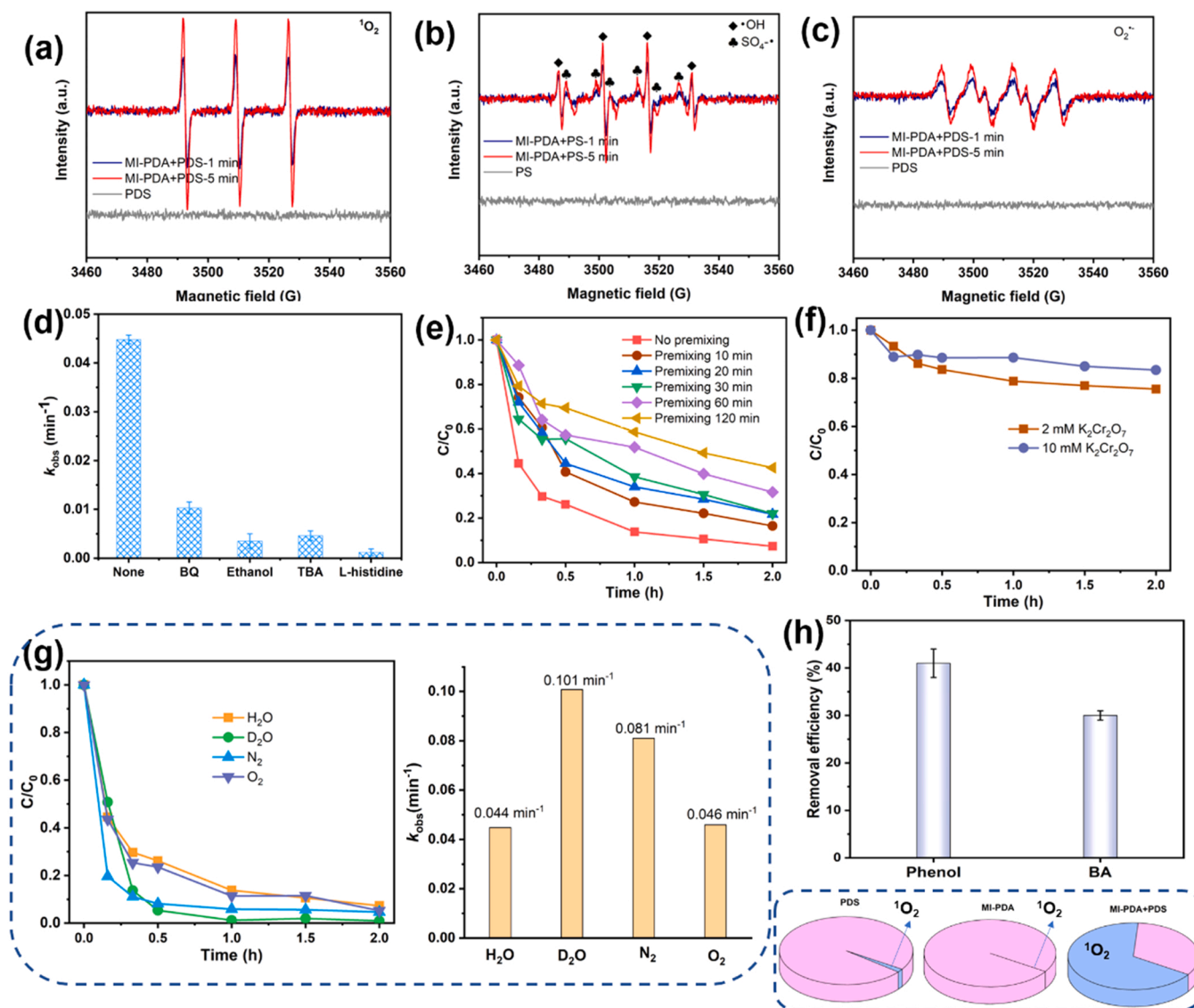
Fig. 4. (a) EPR signals of $^1O_2$, (b) $SO_4^{\bullet-}$ and $\bullet OH$, (c) $O_2^{\bullet-}$. (d) Comparison of reaction rate constant (k_{obs}) of MI-PDA activating PDS in the presence of various scavengers, [BQ]= 10 mM, [EtOH]= 100 mM, [TBA]= 100 mM, [*L*-histidine] = 500 mM. (e) Premixing MI-PDA and PDS on SMX degradation. (f) Effect of ROS inhibition on degradation efficiency. (g) Comparison of degradation kinetics in D_2O, N_2, and O_2 with the MI-PDA/PDS system. (h) Removal efficiency of phenol and BA, quantitative determination of $^1O_2$. Reaction conditions: [SMX] = 0.4 mM, [Catalyst] = 0.5 g/L, [PDS] = 2 mM, T = 25 °C, initial pH = 6.8.

during the process of MI-PDA activating PDS. The exposures rate of PDS increased continuously (Fig. S21a). The exposures rate of $SO_4^{\bullet-}$, $\bullet OH$, and $^1O_2$ were 0.6×10^{-4}, 0.7×10^{-4}, and 0.1×10^{-3} s^{-1} when the added PDS (2 mM) was largely depleted during the MI-PDA/PDS process. The exposures rate of $^1O_2$ was slightly higher than that of $SO_4^{\bullet-}$ and $\bullet OH$ (Fig. S21b), indicating the priority role of $^1O_2$. Above all, $^1O_2$ is dominated in the process of MI-PDA activating PDS and radical ($SO_4^{\bullet-}$, $\bullet OH$) is assistant.

3.5. Mechanistic insights into singlet oxygen generation

A lot of study reported that the PDA can promote catalyst to activate persulfate due to the oxygen-containing functional groups [33], and the generated ROS are generally radicals (Fig. S22). However, the $^1O_2$ can be tested in the MI-PDA/PDS system, suggesting a new insight into MI-PDA activating PDS. Significantly, the masking of oxygen-containing functional groups did not completely inhibit SMX degradation (Fig. S23), indicating the PDS can be activated by other structures in PDA to induce the $^1O_2$ generation. As shown in Fig. 5a, the selective

re-bonding property relies on the hydrogen bond between the -NH$_2$ of SMX and the nitrogenous and -OH of MI-PDA because the intensity of absorption peaks corresponding to nitrogenous groups (1250 cm^{-1} and 1500 cm^{-1}) and hydroxyl groups (3200–3500 cm^{-1}) gradually decreased with adsorption time [47], The nitrogenous groups and oxygen-containing groups of MI-PDA are acted as the recognition site. For the process of PDS activation, Fig. 5b shows that the peak intensity of -NH$_2$ (400.7 eV) increased, and that of -N $=$ (399.1 eV) and -NH- (400.0 eV) decreased [48,49], indicative of the key role of N sites in MI-PDA. Meanwhile, the *in-situ* ATR-FTIR monitored the group changes of MI-PDA during activating PDS. The intensity of the -NH-/-OH peak located at 3200–3500 cm^{-1} decreases as reaction time, especially, the peak intensity of the C-N bond at 1250 cm^{-1} increases firstly and then decreases, which is ascribed to the SMX degradation and then re-adsorption of SMX by recognition sites (Fig. 5c). Moreover, the absorption peaks of $S_2O_8^{2-}$ assigned at (870 cm^{-1}) and S$=$O (1105 cm^{-1}) become stronger, which results from the transition of PDS adsorbed on MI-PDA. A new adsorption peak at 1048 cm^{-1} occurred, which is assigned to the S-O bond [50], indicating that the N sites are significant
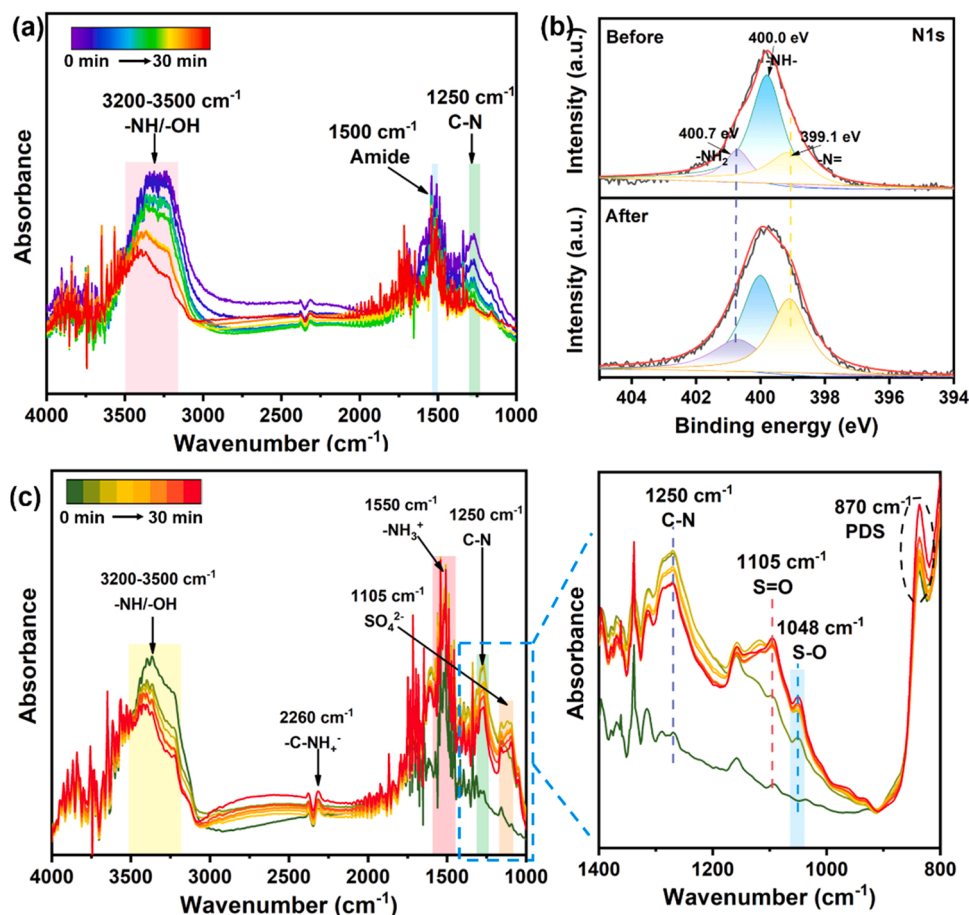
Fig. 5. (a) *In-situ* ATR-FTIR spectrum of adsorption for SMX on MI-PDA. (b) Changes of XPS N1s spectra of MI-PDA before and after used. (c) *In-situ* ATR-FTIR spectrum of degradation for SMX in MI-PDA/PDS system.

for PDS activation. The N sites can retain the stability during the catalytic activation of PDS although it took part in the activation of PDS, which can be testified by the almost unchanged atomic ratio of N to O about 0.4 (Fig. S24).

To further confirm the active sites in MI-PDA for the activation of PDS, the changes in the electron density distribution between the PDS
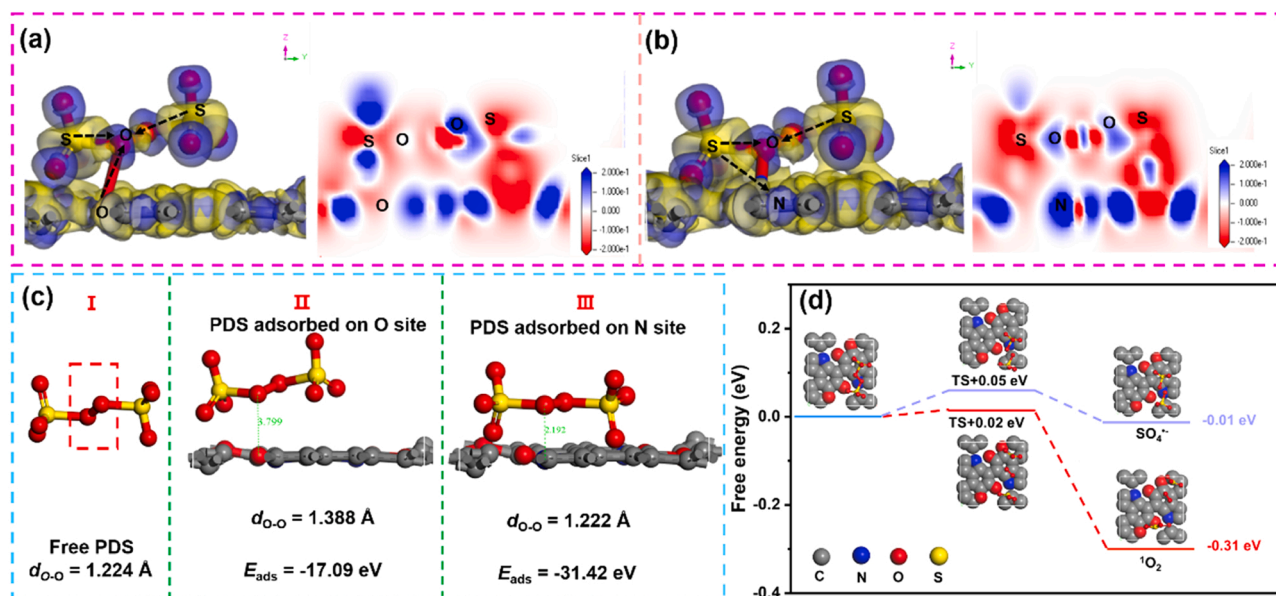

Fig. 6. EDD analysis and 2D images for PDS adsorbed on O sites (a) and N sites (b), where the blue and yellow isosurfaces represent accumulation and depletion, respectively. (c) Energetic and geometric data of the models of (I) free PDS, (II) PDS on O sites, (III) PDS on N sites. (d) Proposed mechanism of $^1O_2$ generation in MI-PDA/PDS system.

and MI-PDA fragment were then studied using electron density difference (EDD) analysis. The electronic densities largely redistribute from the O atom of MI-PDA fragment to the O atom of $S_2O_8^{-}$, indicating that PDS adsorb onto the O sites of the MI-PDA fragment. Many previous literatures reported that the electron-rich O sites in carbon materials can donate electrons to directly decompose PDS to produce $SO_4^{\bullet-}$, which is consistent with the previous study [51]. Notably, we can observe the electronic redistributions from the S atom to the N atom in MI-PDA fragment and the O atom in PDS, resulting in the S-O bond cleavage to generate $^1O_2$. The 2D image of EED has clearly displayed the transport of electron between S, O, and N atoms. Moreover, the adsorption energy of PDS on O and N sites in MI-PDA was calculated to further understand the activation process. As seen in Fig. 6c, with the PDS adsorption on the O site of MI-PDA, the O-O bond length (l_{O-O}) of PDS is stretched (II) and the S-O bond therewith is shrunk compared to that in free PDS (I), contributing to the $SO_4^{\bullet-}$ generation. While the l_{O-O} of PDS is shortened and the S-O bond therewith is elongated as the PDS absorption on N site (III), indicative of the trend of $^1O_2$ generation. Significantly, the adsorption energy ($E_{ads} = E_{MI-PDA+PDS} - E_{MI-PDA} - E_{PDS}$) of PDS on N site ($-31.42$ eV) is higher than that on O site (-17.09 eV) (Fig. 6c), suggesting the preferential generation of $^1O_2$. Hence, the electron redistribution from O atom in MI-PDA to the S atom of $S_2O_8^{2-}$ lead to the O-O bond rupture to generate the $SO_4^{\bullet-}$ [33]. While the direct electron transfer from S atom of $S_2O_8^{2-}$ to the N atom of MI-PDA can induce the S-O bond cleavage, facilitating to the $^1O_2$ produce. The adsorbed PDS may transfer electron to $-NH^+-/=N-$ with higher transient oxidation state, and then these sites can oxidate PDS to generate $^1O_2$ [50], which can be testified by the N species varication in Fig. 5b. Fig. 6d shows that the free energy of $^1O_2$ generation is higher than that of $SO_4^{\bullet-}$ (Fig. S25), indicating that the $^1O_2$ generated by N site activating PDS is dominant in MI-PDA/PDS system, and this process is spontaneous and thermodynamically favorable. The amino on the benzene ring and the sulfamide group in the SMX are was vulnerable to electrophilic and nucleophile attack, respectively [17]. Hence, free radicals ($SO_4^{\bullet-}$ and $\bullet OH$) and non-free radicals ($^1O_2$) would attack the different structures of SMX to ensure the efficient degradation (Fig. S26). The Ecological Structure-Activity Relationship (ECOSAR) class program (ECOSAR v2.2, EPA) was utilized to predict the acute toxicity (Oral rat LC_{50}) of the intermediates [52,53]. As shown in Fig. S27, the degradation products are not harmful (LC50 > 100 mg/L). As such, it can be concluded that MI-PDA molecularly imprinted catalysis not only efficiently removed water contaminants by *in-situ* activating PDS but also significantly weakened the toxicity of intermediates.

3.6. Stability and practical application of catalyst

MI-PDA exhibits exciting stability in morphology and chemical structure after activating PDS (Fig. S28 and Fig. S29). The selective re-bonding and catalytic durability were also investigated as shown in Fig. S30. The adsorption performance has no obvious decay, and the catalytic activity still retained above 71% after four consecutive cycles, implying its favorable stability. In the water matrix, the inorganic anions (Cl^-, NO_3^-) have no effect on SMX degradation in the MI-PDA/PDS system, however, the CO_3^{2-}, HCO_3^- inhibited the SMX removal (Fig. S31), which is because HCO_3^- and CO_3^{2-} could act as scavengers to quench $\bullet OH$ and $SO_4^{\bullet-}$ (Eqs. (1–4)) [54–56]. Interestingly, MI-PDA/PDS system show outstanding adaptability under different concentration of HA (Fig. S32). In addition, the influence of pH on SMX degradation was investigated, and found that the strong alkali environment is not conducive to the activation of PDS (Fig. S33) [57–59].

$$HCO_3^- + \bullet OH \rightarrow CO_3^{\bullet-} + H_2O \tag{1}$$

$$CO_3^{2-} + \bullet OH \rightarrow CO_3^{\bullet-} + OH^- \tag{2}$$

$$HCO_3^- + SO_4^{\bullet-} \rightarrow HCO_3^{\bullet} + SO_4^{2-} \tag{3}$$

$$CO_3^{2-} + SO_4^{\bullet-} \rightarrow CO_3^{\bullet-} + SO_4^{2-} \tag{4}$$

Given the application feasibility of selective recognition site and catalytic performance of the MI-PDA in the actual water sample, the practical application test of NI-PDA/PDS and MI-PDA/PDS systems were conducted (Fig. S34 and Fig. S35). The more efficient degradation of SMX in MI-PDA/PDS system for treating the actual water sample (water quality parameters are shown in Table S2) compared to NI-PDA/PDS system indicate the irreplaceable role of targeted enrichment and *in-situ* catalysis potential of molecularly imprinted polymers. Therefore, MI-PDA can be an alternative and green catalyst for activating oxidants to remediate the trace refractory organic pollutants in advanced water treatment.

4. Conclusions

This study put forward a simple and green synthetic method of molecularly imprinted polymer, which omitted the use of crosslinking agent and initiator. Importantly, the molecularly imprinted polymer can *in-situ* activate PDS to generate $^1O_2$ without introducing extra active centers. As a result, the DA can act as a monomer to prepare the molecular imprinting catalyst by self-polymerization. The nitrogenous group and hydroxyl group as the recognition site of MI-PDA play the key role in selective re-bonding the SMX. Moreover, the N site also acted as the active site to activate the PDS. This study demonstrates the role of the neglected N-site of PDA in activating oxidants, and the N site can directly accept the electron from the S atom of PDS, resulting in the S-O bond cleavage to generate $^1O_2$. The specific recognition site and *in-situ* catalytic performance of the N site endow the MI-PDA with more $^1O_2$ generation to targeted removal of SMX in complex water. This work provides a novel strategy for preparing molecular imprinting catalysts for AOPs application, which inspires new ideas of material design to intentionally construct recognition sites for different trace refractory organic pollutants.

CRediT authorship contribution statement

Min Tang: Experimental design and completion, Formal analysis, Data curation, Methodology, Writing – original draft. **Jinquan Wan**: Supervision, Project administration, Methodology, Writing – review & editing. **Yan Wang**: Writing – review & editing, Formal analysis. **Gang Ye**: Formal analysis, Writing – review & editing. **Zhicheng Yan**: Investigation, Formal analysis. **Yongwen Ma**: Formal analysis, Software. **Jian Sun**: Formal analysis, Methodology.

Declaration of Competing Interest

The authors declare that they have no known competing financial interests or personal relationships that could have appeared to influence the work reported in this paper.

Data Availability

No data was used for the research described in the article.

Appendix A. Supporting information

Supplementary data associated with this article can be found in the online version at doi:10.1016/j.apcatb.2023.122852.

References

[1] R. Schwarzenbach, B.I. Escher, K. Fenner, T.B. Hofstetter, C.A. Johnson, U. von Gunten, B. Wehrli, The challenge of micropollutants in aquatic system, Science 313 (2006) 1072–1077.

[2] S. Pei, J. Teng, N. Ren, S. You, Low-temperature removal of refractory organic pollutants by electrochemical oxidation: Role of interfacial joule heating effect, Environ. Sci. Technol. 54 (2020) 4573–4582, https://doi.org/10.1021/acs. est.9b05929.

[3] C. Galbán-Malagón, N. Berrojalbiz, M.J. Ojeda, J. Dachs, The oceanic biological pump modulates the atmospheric transport of persistent organic pollutants to the Arctic, Nat. Commun. 3 (2012) 1–9, https://doi.org/10.1038/ncomms1858.

[4] Y.J. Zhang, J.L. Guo, J. chuan Xue, C.L. Bai, Y. Guo, Phthalate metabolites: characterization, toxicities, global distribution, and exposure assessment, Environ. Pollut. 291 (2021), 118106, https://doi.org/10.1016/j.envpol.2021.118106.

[5] J. Lee, U. Von Gunten, J.H. Kim, Persulfate-based advanced oxidation: critical assessment of opportunities and roadblocks, Environ. Sci. Technol. 54 (2020) 3064–3081, https://doi.org/10.1021/acs.est.9b07082.

[6] Y.Y. Ahn, H. Bae, H. Il Kim, S.H. Kim, J.H. Kim, S.G. Lee, J. Lee, Surface-loaded metal nanoparticles for peroxymonosulfate activation: efficiency and mechanism reconnaissance, Appl. Catal. B Environ. 241 (2019) 561–569, https://doi.org/10.1016/j.apcatb.2018.09.056.

[7] P. Zhang, Y. Yang, X. Duan, Y. Liu, S. Wang, Density functional theory calculations for insight into the heterocatalyst reactivity and mechanism in persulfate-based advanced oxidation reactions, ACS Catal. 11 (2021) 11129–11159, https://doi.org/10.1021/acscatal.1c03099.

[8] F. Liu, Y. Zhang, S. Wang, T. Gong, M. Hua, J. Qian, B. Pan, Metal-free biomass with abundant carbonyl groups as efficient catalyst for the activation of peroxymonosulfate and degradation of sulfamethoxazole, Chem. Eng. J. 430 (2022), 132767, https://doi.org/10.1016/j.cej.2021.132767.

[9] P. Shao, S. Yu, X. Duan, L. Yang, H. Shi, L. Ding, J. Tian, L. Yang, X. Luo, S. Wang, Potential difference driving electron transfer via defective carbon nanotubes toward selective oxidation of organic micropollutants, Environ. Sci. Technol. 54 (2020) 8464–8472, https://doi.org/10.1021/acs.est.0c02645.

[10] L. Bo, H. Liu, H. Han, Photocatalytic degradation of trace carbamazepine in river water under solar irradiation, J. Environ. Manag. 241 (2019) 131–137, https://doi.org/10.1016/j.jenvman.2019.03.132.

[11] J. Yang, M. Zhu, D.D. Dionysiou, What is the role of light in persulfate-based advanced oxidation for water treatment? Water Res 189 (2021), 116627 https://doi.org/10.1016/j.watres.2020.116627.

[12] S. Xiao, M. Cheng, H. Zhong, Z. Liu, Y. Liu, X. Yang, Q. Liang, Iron-mediated activation of persulfate and peroxymonosulfate in both homogeneous and heterogeneous ways: a review, Chem. Eng. J. 384 (2020) 123265, https://doi.org/10.1016/j.cej.2019.123265.

[13] J. Zhang, B. Tang, G. Zhao, Selective photoelectrocatalytic removal of dimethyl phthalate on high-quality expressed molecular imprints decorated specific facet of single crystalline TiO2 photoanode, Appl. Catal. B Environ. 279 (2020) 119364, https://doi.org/10.1016/j.apcatb.2020.119364.

[14] C. Zeng, Y. Wang, T. Xiao, Z. Yan, J. Wan, Q. Xie, Targeted degradation of TBBPA using novel molecularly imprinted polymer encapsulated C-Fe-Nx nanocomposite driven from MOFs, J. Hazard. Mater. 424 (2022) 127499, https://doi.org/10.1016/j.jhazmat.2021.127499.

[15] X. Li, B. Yang, K. Xiao, H. Duan, J. Wan, H. Zhao, Targeted degradation of refractory organic compounds in wastewaters based on molecular imprinting catalysts, Water Res. 203 (2021), 117541, https://doi.org/10.1016/j.watres.2021.117541.

[16] Q. Li, Y. Huang, Z. Pan, J. Ni, W. Yang, J. Chen, Hollow C, N-TiO2 @ C surface molecularly imprinted microspheres with visible light photocatalytic regeneration availability for targeted degradation of sulfadiazine, Sep. Purif. Technol. 299 (2022), 121814, https://doi.org/10.1016/j.seppur.2022.121814.

[17] Y. Xie, J. Wan, Z. Yan, Y. Wang, T. Xiao, J. Hou, H. Chen, Targeted degradation of sulfamethoxazole in wastewater by molecularly imprinted MOFs in advanced oxidation processes: degradation pathways and mechanism, Chem. Eng. J. 429 (2022), 132237, https://doi.org/10.1016/j.cej.2021.132237.

[18] C.C. de Escobar, M.A. Lansarin, J.H. Zimnoch, dos Santos, Synthesis of molecularly imprinted photocatalysts containing low TiO2 loading: Evaluation for the degradation of pharmaceuticals, J. Hazard. Mater. 306 (2016) 359–366, https://doi.org/10.1016/j.jhazmat.2015.11.035.

[19] J. Wang, J. Feng, C. Wei, Molecularly imprinted polyaniline immobilized on Fe3O4/ZnO composite for selective degradation of amoxycillin under visible light irradiation, Appl. Surf. Sci. 609 (2023), 155324, https://doi.org/10.1016/j.apsusc.2022.155324.

[20] X. Li, J. Wan, Y. Wang, Z. Yan, H. Chi, S. Ding, Mechanism of accurate recognition and catalysis of diethyl phthalate (DEP) in wastewater by novel MIL100 molecularly imprinted materials, Appl. Catal. B Environ. 266 (2020), 118591, https://doi.org/10.1016/j.apcatb.2020.118591.

[21] Q. Yuan, D. Zhang, P. Yu, R. Sun, H. Javed, G. Wu, P.J.J. Alvarez, Selective adsorption and photocatalyticdegradation of extracellular antibiotic resistance genes by molecularly-imprinted graphitic carbon nitride, Environ. Sci. Technol. 54 (2020) 4621–4630, https://doi.org/10.1021/acs.est.9b06926.

[22] Z. Zhang, X. Zhang, B. Liu, J. Liu, Molecular imprinting on inorganic nanozymes for hundred-fold enzyme specificity, J. Am. Chem. Soc. 139 (2017) 5412–5419, https://doi.org/10.1021/jacs.7b00601.

[23] M. Yoshikawa, K. Tharpa, Ş.O. Dima, Molecularly imprinted membranes: past, present, and future, Chem. Rev. 116 (2016) 11500–11528, https://doi.org/10.1021/acs.chemrev.6b00098.

[24] W. Zhang, Y. Zhang, R. Wang, P. Zhang, Y. Zhang, E. Randell, M. Zhang, Q. Jia, A review: development and application of surface molecularly imprinted polymers toward amino acids, peptides, and proteins, Anal. Chim. Acta 1234 (2022), 340319, https://doi.org/10.1016/j.aca.2022.340319.

[25] K. Poonia, P. Raizada, A. Singh, N. Verma, T. Ahamad, S.M. Alshehri, A.A.P. Khan, P. Singh, C.M. Hussain, Magnetic molecularly imprinted polymer photocatalysts: synthesis, applications and future perspective, J. Ind. Eng. Chem. 113 (2022) 1–14, https://doi.org/10.1016/j.jiec.2022.05.029.

[26] Y. Zamrodah, Mussel-inspired surface chemistry for multifunctional coatings, Science 318 (2007) 426–430.

[27] F. Wu, N. Pu, G. Ye, T. Sun, Z. Wang, Y. Song, W. Wang, X. Huo, Y. Lu, J. Chen, Performance and mechanism of uranium adsorption from seawater to poly (dopamine)-inspired sorbents, Environ. Sci. Technol. 51 (2017) 4606–4614, https://doi.org/10.1021/acs.est.7b00470.

[28] X. Wang, Z. Liu, J. Lu, H. Teng, H. Fukuda, Highly selective membrane for efficient separation of environmental determinands: Enhanced molecular imprinting in polydopamine-embedded porous sleeve, Chem. Eng. J. 449 (2022), 137825, https://doi.org/10.1016/j.cej.2022.137825.

[29] C. Wang, L. Liu, J. Lu, H. Teng, H. Fukuda, L. Zhang, W. Tang, C. Dong, D. Zhou, X. Xing, W. Dong, Y. Ding, G. Wang, M. Wu, Bionic sunflower-like structure of polydopamine-confined NiFe-based quantum dots for electrocatalytic oxygen evolution reaction, Appl. Catal. B Environ. 302 (2022), 120833, https://doi.org/10.1016/j.apcatb.2021.120833.

[30] Y. Liu, K. Ai, L. Lu, Polydopamine and its derivative materials: Synthesis and promising applications in energy, environmental, and biomedical fields, Chem. Rev. 114 (2014) 5057–5115, https://doi.org/10.1021/cr400407a.

[31] W. Cheng, X. Zeng, H. Chen, Z. Li, W. Zeng, L. Mei, Y. Zhao, Versatile polydopamine platforms: Synthesis and promising applications for surface modification and advanced nanomedicine, ACS Nano 13 (2019) 8537–8565, https://doi.org/10.1021/acsnano.9b04436.

[32] C. Liu, Q. He, D. Song, J. Jackson, A.F. Faria, X. Jiang, X. Li, J. Ma, Z. Sun, Electroless deposition of copper nanoparticles integrates polydopamine coating on reverse osmosis membranes for efficient biofouling mitigation, Water Res 217 (2022), 118375, https://doi.org/10.1016/j.watres.2022.118375.

[33] X. Li, K. Liang, B. Yang, K. Xiao, H. Duan, G. Song, H. Zhao, Preparation and application of a targeted magnetically separated catalyst for sulfonamides degradation based on molecular dynamics selection and mechanism analysis, Chem. Eng. J. 432 (2022), 134365, https://doi.org/10.1016/j.cej.2021.134365.

[34] Q. He, J.J. Liang, L.X. Chen, S.L. Chen, H.L. Zheng, H.X. Liu, H.J. Zhang, Removal of the environmental pollutant carbamazepine using molecular imprinted adsorbents: molecular simulation, adsorption properties, and mechanisms, Water Res 168 (2020), 115164, https://doi.org/10.1016/j.watres.2019.115164.

[35] Z. Sun, L. Zhao, C. Liu, Y. Zhen, J. Ma, Fast adsorption of BPA with high capacity based on π-π electron donor-acceptor and hydrophobicity mechanism using an in-situ sp2C dominant N-doped carbon, Chem. Eng. J. 381 (2020), 122510, https://doi.org/10.1016/j.cej.2019.122510.

[36] X. Zhang, X. Zhang, Y. Cai, S. Wang, Peroxymonosulfate-activated molecularly imprinted bimetallic MOFs for targeted removal of PAHs and recovery of biosurfactants from soil washing effluents, Chem. Eng. J. 443 (2022), 136412, https://doi.org/10.1016/j.cej.2022.136412.

[37] M. Tang, J. Wan, Y. Wang, Z. Yan, Y. Ma, J. Sun, S. Ding, Developing a molecularly imprinted channels catalyst based on template effect for targeted removal of organic micropollutants from wastewaters, Chem. Eng. J. 445 (2022), 136755, https://doi.org/10.1016/j.cej.2022.136755.

[38] L. Gao, Y. Guo, J. Zhan, G. Yu, Y. Wang, Assessment of the validity of the quenching method for evaluating the role of reactive species in pollutant abatement during the persulfate-based process, Water Res 221 (2022), 118730, https://doi.org/10.1016/j.watres.2022.118730.

[39] L. Gao, Y. Guo, J. Huang, B. Wang, S. Deng, G. Yu, Y. Wang, Simulating micropollutant abatement during cobalt mediated peroxymonosulfate process by probe-based kinetic models, Chem. Eng. J. 441 (2022), 135970, https://doi.org/10.1016/j.cej.2022.135970.

[40] Y. Gao, Z. Chen, Y. Zhu, T. Li, C. Hu, New insights into the generation of singlet oxygen in the metal-free peroxymonosulfate activation process: important role of electron-deficient carbon atoms, Environ. Sci. Technol. 54 (2020) 1232–1241, https://doi.org/10.1021/acs.est.9b05856.

[41] W. Ren, C. Cheng, P. Shao, X. Luo, H. Zhang, S. Wang, X. Duan, Origins of electron-transfer regime in persulfate-based nonradical oxidation processes, Environ. Sci. Technol. 56 (2022) 78–97, https://doi.org/10.1021/acs.est.1c05374.

[42] P. Duan, J. Pan, W. Du, Q. Yue, B. Gao, X. Xu, Activation of peroxymonosulfate via mediated electron transfer mechanism on single-atom Fe catalyst for effective organic pollutants removal, Appl. Catal. B Environ. 299 (2021), 120714, https://doi.org/10.1016/j.apcatb.2021.120714.

[43] P. Shao, Y. Jing, X. Duan, H. Lin, L. Yang, W. Ren, F. Deng, B. Li, X. Luo, S. Wang, Revisiting the graphitized nanodiamond-mediated activation of peroxymonosulfate: singlet oxygenation versus electron transfer, Environ. Sci. Technol. 55 (2021) 16078–16087, https://doi.org/10.1021/acs.est.1c02042.

[44] C.M. Morton, Q. Zhu, H. Ripberger, L. Troian-Gautier, Z.S.D. Toa, R.R. Knowles, E. J. Alexanian, C-H alkylation via multisite-proton-coupled electron transfer of an aliphatic C-H bond, J. Am. Chem. Soc. 141 (2019) 13253–13260, https://doi.org/10.1021/jacs.9b06834.

[45] Y. Yao, C. Wang, Y. Yan, H. Zhang, C. Xiao, J. Qi, Z. Zhu, Y. Zhou, X. Sun, X. Duan, J. Li, Rational regulation of Co-N-C coordination for high-efficiency generation of ¹O₂ toward nearly 100% selective degradation of organic pollutants, Environ. Sci. Technol. 56 (2022) 8833–8843, https://doi.org/10.1021/acs.est.2c00706.

[46] R. Gao, X. Mei, D. Yan, R. Liang, M. Wei, Nano-photosensitizer based on layered double hydroxide and isophthalic acid for singlet oxygenation and photodynamic

therapy, Nat. Commun. 9 (2018) 1–10, https://doi.org/10.1038/s41467-018-05223-3.

[47] W. Ye, X. Shi, J. Su, Y. Chen, J. Fu, X. Zhao, F. Zhou, C. Wang, D. Xue, One-step reduction and functionalization protocol to synthesize polydopamine wrapping Ag/graphene hybrid for efficient oxidation of hydroquinone to benzoquinone, Appl. Catal. B Environ. 160–161 (2014) 400–407, https://doi.org/10.1016/j.apcatb.2014.05.042.

[48] A. Meng, B. Cheng, H. Tan, J. Fan, C. Su, J. Yu, TiO$_2$/polydopamine S-scheme heterojunction photocatalyst with enhanced CO$_2$-reduction selectivity, Appl. Catal. B Environ. 289 (2021), 120039, https://doi.org/10.1016/j.apcatb.2021.120039.

[49] F. Chen, L. Zhao, W. Yu, Y. Wang, H. Zhang, L.H. Guo, Dynamic monitoring and regulation of pentachlorophenol photodegradation process by chemiluminescence and TiO$_2$/PDA, J. Hazard. Mater. 399 (2020), 123073, https://doi.org/10.1016/j.jhazmat.2020.123073.

[50] Y. Zhao, L. Yu, C. Song, Z. Chen, F. Meng, M. Song, Selective degradation of electron-rich organic pollutants induced by CuO@biochar: The key role of outer-sphere interaction and singlet oxygen, Environ. Sci. Technol. 56 (2022) 10710–10720, https://doi.org/10.1021/acs.est.2c01759.

[51] P. Zhang, P. Zhou, J. Peng, Y. Liu, H. Zhang, C. He, Z. Xiong, W. Liu, B. Lai, Insight into metal-free carbon catalysis in enhanced permanganate oxidation: changeover from electron donor to electron mediator, Water Res 219 (2022), 118626, https://doi.org/10.1016/j.watres.2022.118626.

[52] C. Meng, B. Ding, S. Zhang, L. Cui, K.K. Ostrikov, Z. Huang, B. Yang, J.H. Kim, Z. Zhang, Angstrom-confined catalytic water purification within Co-TiOx laminar membrane nanochannels, Nat. Commun. 13 (2022) 1–10, https://doi.org/10.1038/s41467-022-31807-1.

[53] J. Wang, D. Zhi, H. Zhou, X. He, D. Zhang, Evaluating tetracycline degradation pathway and intermediate toxicity during the electrochemical oxidation over a Ti/Ti$_4$O$_7$ anode, Water Res 137 (2018) 324–334, https://doi.org/10.1016/j.watres.2018.03.030.

[54] S. Yang, D. Tian, X. Wang, P. Zhou, Z. Xiong, H. Zhang, Y. Liu, G. Yao, B. Lai, The enhanced mechanism of Fe(III)/H$_2$O$_2$ system by N, S-doped mesoporous nanocarbon for the degradation of sulfamethoxazole, Sep. Purif. Technol. 308 (2023), 122900, https://doi.org/10.1016/j.seppur.2022.122900.

[55] Z. Wu, Y. Wang, Z. Xiong, Z. Ao, S. Pu, G. Yao, B. Lai, Core-shell magnetic Fe$_3$O$_4$@Zn/Co-ZIFs to activate peroxymonosulfate for highly efficient degradation of carbamazepine, Appl. Catal. B Environ. 277 (2020), 119136, https://doi.org/10.1016/j.apcatb.2020.119136.

[56] S. Giannakis, K.Y.A. Lin, F. Ghanbari, A review of the recent advances on the treatment of industrial wastewaters by Sulfate Radical-based Advanced Oxidation Processes (SR-AOPs), Chem. Eng. J. 406 (2021), 127083, https://doi.org/10.1016/j.cej.2020.127083.

[57] J. Wang, S. Wang, Effect of inorganic anions on the performance of advanced oxidation processes for degradation of organic contaminants, Chem. Eng. J. 411 (2021), 128392, https://doi.org/10.1016/j.cej.2020.128392.

[58] A. Fernandes, P. Makoś, G. Boczkaj, Treatment of bitumen post oxidative effluents by sulfate radicals based advanced oxidation processes (S-AOPs) under alkaline pH conditions, J. Clean. Prod. 195 (2018) 374–384, https://doi.org/10.1016/j.jclepro.2018.05.207.

[59] J. Wang, S. Wang, Reactive species in advanced oxidation processes: formation, identification and reaction mechanism, Chem. Eng. J. 401 (2020), 126158, https://doi.org/10.1016/j.cej.2020.126158.